[^{18}F]Galacto-RGD Positron Emission Tomography for Imaging of $\alpha v\beta 3$ Expression on the Neovasculature in Patients with Squamous Cell Carcinoma of the Head and Neck

Ambros J. Beer,[1] Anca-Ligia Grosu,[2] Janette Carlsen,[1] Andreas Kolk,[3] Mario Sarbia,[4] Isabelle Stangier,[1] Petra Watzlowik,[1] Hans-Jürgen Wester,[1] Roland Haubner,[5] and Markus Schwaiger[1]

Abstract

Purpose: [^{18}F]Galacto-RGD has been developed for positron emission tomography (PET)–imaging of $\alpha v\beta 3$ expression, a receptor involved in angiogenesis and metastasis. Our aim was to study the feasibility of PET imaging with [^{18}F]Galacto-RGD in patients with squamous cell carcinoma of the head and neck (SCCHN).

Experimental Design: Eleven patients with primary diagnosis of SCCHN were examined. After injection of 140 to 200 MBq [^{18}F]Galacto-RGD, static emission scans 60 min post injection from the head to the abdomen ($n = 11$) and dynamic scans ›60 min covering the tumor region ($n = 6$) for kinetic modeling were acquired. Standardized uptake values (SUV) were measured in tumors, muscle and oral mucosa. Immunohistochemistry was done using an $\alpha v\beta 3$-specific antibody ($n = 7$). Image fusion with magnetic resonance imaging and/or computed tomography (CT) scans ($n = 8$) and calculation of tumor subvolumes based on SUVs was done using the iPlan software (BrainLAB).

Results: [^{18}F]Galacto-RGD PET identified 10 of 12 tumors, with SUVs ranging from 2.2 to 5.8 (mean, 3.4 $\pm$ 1.2). Two tumors ‹5 mm were missed. Tumor/blood and tumor/muscle ratios were 2.8 $\pm$ 1.1 and 5.5 $\pm$ 1.6, respectively. Tumor kinetics was consistent with a two-tissue compartmental model with reversible specific binding. Immunohistochemistry confirmed $\alpha v\beta 3$ expression in all tumors with $\alpha v\beta 3$ being located on the microvessels in all specimens and additionally on tumor cells in one specimen. Image fusion of [^{18}F]Galacto-RGD PET with magnetic resonance imaging/multislice CT and definition of tumor subvolumes was feasible in all cases.

Conclusions: [^{18}F]Galacto-RGD PET allows for specific imaging of $\alpha v\beta 3$ expression in SCCHN with good contrast. Image fusion and definition of tumor subvolumes is feasible. This technique might be used for the assessment of angiogenesis and for planning and response evaluation of $\alpha v\beta 3$-targeted therapies.

Recently, encouraging results have been achieved with anti-angiogenic drugs like the vascular endothelial growth factor antibody bevacizumab (Avastin) in combination with standard cytotoxic chemotherapy in metastasized colorectal cancer, breast cancer, and non–small cell lung cancer (1, 2). Moreover, agents targeting angiogenesis are promising for lowering the toxicity of conventional chemoradiotherapy (3–6). This approach has been shown to enhance tissue oxygenation, susceptibility of microvessels, and tumor growth delay during radiotherapy in preclinical studies (7, 8). First results from patient studies with various advanced tumors including squamous cell cancer of the head and neck (SCCHN) using angiostatin in combination with radiotherapy showed that this regimen is safe, did not increase radiation-induced toxicity, and produced durable local tumor responses (9). These encouraging results suggest that the use of targeted agents, in combination with conventional chemotherapy or radiotherapy, will increase in the future. This will also spur the demand for methods for planning these therapies by selecting the right patient group and for controlling therapeutic success by using surrogate variables. Molecular imaging targeting specific pathways involved in angiogenesis lends itself for this purpose, as it is noninvasive and can be easily repeated during the course of therapy. Integrin $\alpha v\beta 3$ is an interesting target in this respect, as it is highly expressed in activated endothelial cells during angiogenesis and plays an important role in the regulation of tumor growth, local invasiveness, and metastatic potential

Authors' Affiliations: Departments of [1]Nuclear Medicine, [2]Radiation Therapy, [3]Cranio-Maxillofacial Surgery, and [4]Pathology, Technische Universität München, Munich, Germany; and [5]Universitätsklinik für Nuklearmedizin, Medizinische Universität Innsbruck, Innsbruck, Austria

Received 3/5/07; revised 7/3/07; accepted 9/7/07.

Grant support: Münchner Medizinische Wochenschrift and the Sander-Foundation.

The costs of publication of this article were defrayed in part by the payment of page charges. This article must therefore be hereby marked *advertisement* in accordance with 18 U.S.C. Section 1734 solely to indicate this fact.

Note: A.J. Beer and A-L. Grosu contributed equally to this work. Current address for M. Sarbia: Unfallkrankenhaus Berlin, Institut für Pathologie, Berlin, Germany. Current Address for A-L. Grosu: Department of Radiation Oncology, University Hospital Freiburg, Freiburg, Germany.

Requests for reprints: Ambros J. Beer, Department of Nuclear Medicine, Technische Universität München, Klinikum rechts der Isar, Ismaninger Str. 22, 81675 Munich, Germany. Phone: 49-89-4140-2971; Fax: 49-89-4140-4950; E-mail: beer@roe.med.tum.de.

doi:10.1158/1078-0432.CCR-07-0528

(10, 11). Moreover, αvβ3 antagonists like EMD 121974 [cyclo-L-Arg-Gly-L-Asp-D-Phe-N (Me) L-Val; Cilengitide] have been shown to enhance the efficacy of radiotherapy in preclinical studies (12). We have therefore developed the radiotracer [^{18}F]Galacto-RGD for imaging of αvβ3 expression using positron emission tomography (PET; ref. 13). It has already been shown that this tracer allows for specific imaging of αvβ3 expression in humans with good contrast and with a low radiation dose, comparable to [^{18}F]FDG (14, 15). Moreover, it has been shown that the intensity of [^{18}F]Galacto-RGD uptake correlates with αvβ3 expression in murine tumor xenografts as well as in patients with cancer (16, 17). As the next step, we are now focusing on specific tumor entities to evaluate the clinical use of [^{18}F]Galacto-RGD PET. SCCHN is an interesting tumor in this respect, as it is known to be highly vascularized and is frequently treated with radiation therapy or combined chemo-radiotherapy in advanced stages. Moreover, several studies have shown the correlation between neovascularization and prognosis in patients with SCCHN (18–20).

The purpose of this study was to prove the feasibility of PET imaging of αvβ3 expression in patients with SCCHN using [^{18}F]Galacto-RGD and to show that image quality was sufficient for image fusion with conventional imaging methods such as magnetic resonance imaging (MRI) and/or computed tomography (CT), which facilitates its potential use for biological target volume definition in radiation therapy planning. Moreover, we studied the pharmacokinetics of [^{18}F]Galacto-RGD in SCCHN to prove the specificity of tracer accumulation. Finally, we analyzed the patterns of αvβ3 expression in SCCHN using immunohistochemistry to evaluate if αvβ3 is predominantly expressed on the endothelium of the neovasculature or to a substantial amount on the tumor cells themselves, as this might limit the use of αvβ3 as a pure marker of angiogenesis.

Materials and Methods

Radiopharmaceutical preparation

Synthesis of the labeling precursor and subsequent [^{18}F]-labeling were carried out as described previously (21). The integrity of [^{18}F]Galacto-RGD was controlled by reversed-phase high-performance liquid chromatography before injection for every synthesis. The radiochemical purity was always >98%. The specific activity was between 40 and 100 TBq/mmol. The injected activity per patient was between 140 and 200 MBq. The IC_{50} values for the cold reference compound have been determined and published previously (13). The cyclic pentapeptide has a defined structure mainly determined by the D-amino acid in the sequence, and thus, no variances in binding affinities are expected. Although the assessment of binding affinity was not done for every synthesis, we do not think that the structure of the peptide shows any variances in different synthesis.

Patients

The study was approved by the ethics committee of the Technische Universität München and informed written consent was obtained from all patients. Eleven patients were included in the study and examined between March 2004 and May 2006 (two females, nine males; age, 53.7 ± 8.9 years; range, 35-63 years). Inclusion criteria consisted of biopsy proven or suspected SCCHN scheduled for surgery or radiotherapy as determined by MRI and/or CT, age >18 years, and the ability to give written and informed consent. Exclusion criteria consisted of pregnancy, lactation period, and impaired renal function (serum creatinine level, >1.2 mg/dL). The patient data are summarized in Table 1.

Conventional imaging

All patients had conventional morphologic imaging either as MRI (n = 7) and/or multislice CT (MSCT, n = 7) with the head in the same position as in the PET scanner with the arms down. The MRI examinations were done with a 1.5 T Gyroscan Intera scanner using a phased array surface coil (Philips) using the following sequences with a slice thickness of 5 mm and a slice gap of 0.5 mm:

- STIR coronal plane: TR (repetition time) = 4321, TE (echo time) = 90 ms, TI (inversion time) = 165 ms.
- STIR axial plane: TR = 5484 ms, TE = 90 ms, TI = 150 ms.
- T1 weighted scans in the axial plane before and after i.v. administration of gadolinium-diethylenetriaminepentaacetic acid at a dose of 0.1 mmol/kg body weight (Magnevist; Schering): TR = 668 ms, TE = 15 ms.
- T1 weighted gadolinium-enhanced scans with fat saturation (Prosat) in the axial and coronal plane: TR = 550 ms, TE = 23 ms.

The MSCT examinations were done with a Sensation 16 MSCT (n = 6) scanner or Biograph Sensation 16 PET/CT scanner, respectively, in one patient who underwent a [^{18}F]FDG-PET/CT scan for staging (Siemens).

Table 1. Patient data

No.	Age	Tumor-node-metastasis stage	Tumor size (cm) max. diameter	SUV tumor	SUV LN	Staining pattern IHC αvβ3*
1	50	pT_1 pN_{2b} cM_0 G_2	0.2	n.d.	4.00	Tumor vessels in lymph node metastasis positive; ++
2	35	pT_3 pN_0 cM_0 G_2	2.0	3.80	—	Tumor vessels positive; +
3	59	pT_1 pN_0 cM_0 G_1	1.4	3.10	—	Tumor vessels positive; +
4	42	mcT_3 cN_0 cM_0 G_3	3.0	5.80	—	Tumor vessels and cells positive; ++
			1.8	3.57	—	
5	61	pT_1 pN_1 cM_0 G_2	1.0	2.38	n.d.	Tumor vessels positive; +
6	59	pT_2 pN_1 cM_0 G_2	4.5	5.26	n.d.	Tumor vessels positive; ++
7	59	pT_2 pN_0 cM_0 G_2	4.0	3.25	—	Tumor vessels positive; ++
8	52	mpT_1 pN_0 cM_0 G_1	0.1/0.3	n.d.	—	
9	63	cT_3 cN_2c cM_0 G_3	2.0	2.75	n.d.	
10	55	cT_3 cN_{2c} cM_1 G_3	3.0	2.20	2.05	
11	58	cT_3 cN_1 cM_0 G_3	3.2	2.30	n.d.	

Abbreviations: LN, lymph node; IHC, immunohistochemistry; n.d., lesion not depicted by [^{18}F]Galacto-RGD PET.
*Overall staining intensity: 0, negative; +, weak; ++, moderate; +++, intense staining.

Contrast medium (120 mL, Imeron 300; Altana) were administered at a flow rate of 3 mL/s, followed by a saline flush of 30 mL at 3 mL/s. The following scan variables were used: collimation 16 × 0.75 mm; tube voltage, 120 kV; tube current, 150 mAs; reconstructed slice thickness, 3 mm; reconstruction increment, 3 mm; for multiplanar reconstructions, isotropic data sets with a slice thickness of 0.75 mm and reconstruction increment of 0.7 mm were calculated as well.

PET imaging procedure

Imaging was done with an ECAT EXACT PET scanner (CTI/Siemens) in all instances. Before injection of [^{18}F]Galacto-RGD (140-200 MBq), a transmission scan was acquired for 5 min per bed position (five bed positions) using three rotating [^{68}Ge] rod sources (each with ~90 MBq [^{68}Ge]). In each subject, a static emission scan was acquired in the caudocranial direction, beginning on average 65 ± 6.9 min after injection of [^{18}F]Galacto-RGD, covering a field of view from the abdomen to the base of the skull (five to seven bed positions, 5 min per bed position). In six patients, dynamic emission scans of 22 frames during 60 min after bolus injection of the tracer were acquired covering the region of the tumor in order to obtain time-activity curves (TAC) in malignant lesions (6 frames × 20 s, 6 frames × 30 s, 5 frames × 60 s, 4 frames × 300 s, and 3 frames × 600 s).

Image analysis

Positron emission data were reconstructed using the ordered subsets expectation maximization algorithm using eight iterations and four subsets. The images were attenuation-corrected using the transmission data collected over the same region of emission imaging. For image analysis, the CAPP software, version 7.1 (CTI/Siemens) was used. The static emissions scans were calibrated to standardized uptake values (SUV), the dynamic scans to Bq/mL. The SUV was calculated according to the following formula: [measured activity concentration (Bq/mL) × body weight (g)] / injected activity (Bq; ref. 22).

Static emission scans. In the static emission scans, circular regions of interest (ROI) with a diameter of 1.5 cm were placed over the left ventricle (for measurement of blood pool activity), the dorsal neck soft tissues (for measurement of muscle tissue activity), the palate (for measurement of oral mucosa activity), and tumor tissue in three adjacent slices by an experienced operator. Results were expressed in mean SUV. In the tumors, the areas with the maximum intensity were chosen for measurements. In tumors with a diameter of <2 cm and visible uptake (n = 3), the SUV might be underestimated due to partial volume effects, therefore, the diameter of the ROI was adapted to the tumor size and the maximum SUV in the ROI was chosen for further analysis (23). Tumor/blood ratios and tumor/muscle ratios were calculated by the following formulas: SUV_{tumor}/SUV_{blood} and SUV_{tumor}/SUV_{muscle}.

Dynamic emission scans and kinetic modeling. The selection of TAC and subsequent kinetic analyses were done using the PMOD Medical Imaging Program version 2.5 (PMOD Group). A ROI approach was applied to the dynamic images in order to obtain TACs for lesions as well as background tissue (muscle) and oral mucosa. In the case of tumor tissue, polygonal ROIs were drawn over the whole tumor in all slices with visible tumor uptake. Circular ROIs with a diameter of 15 mm were drawn over muscle tissue in the whole volume of interest and oral mucosa at the height of the palate. The last frame of the dynamic image series was used to define the ROIs for the tumor, muscle, and oral mucosa. In order to derive an image-based input function, freehand ROIs were placed over the common and internal carotid artery in every slice where the artery could be identified on the frames acquired 40 s postinjection (p.i.). The diameter of the ROIs was adapted to the visible lumen of the vessel and always chosen smaller then the apparent vessel diameter to minimize partial volume effects. All ROIs were then projected onto the complete dynamic data set and TACs were subsequently derived. Results from previous studies confirmed high metabolic stability of [^{18}F]Galacto-RGD with >90% intact tracer until 2 h p.i. (17). Therefore, no correction for metabolites was necessary. As we did not study SCCHN systematically before with [^{18}F]Galacto-RGD PET, the primary goal of our kinetic modeling studies was to evaluate the quality of the tracer dynamics in tumor tissue (i.e., rapid washout, plateau, or tracer accumulation?). However, we did not intend to exactly quantify rate constants or receptor density, because for this purpose, a more invasive approach including arterial blood sampling to generate exact arterial input functions would have been necessary. We have already shown in murine tumor models, as well as in patients, that SUVs from static emission scans allow for an identification of the level of αvβ3 expression (16, 17). However, it has to be stressed that although the concept of image-based arterial input functions from the carotid arteries or intracerebral vessels has been used before, the small diameter of these vessels will lead to substantial partial volume effects, and therefore, an underestimation of the blood pool activity (24, 25). Moreover, spillover from the adjacent veins has to be considered as well. Taken together, these effects will likely cause an attenuated and broadened blood pool TAC. This will lead to an overestimation of the values for K_1 and blood volume. This has to be taken into account when interpreting our results and is a limitation of our study.

Individual rate constants were generated by nonlinear regression analysis using the Marquardt-Levenberg least-squares minimization algorithm as implemented in PMOD. Various compartment models were fitted to the data and kinetic constants were estimated by minimizing the sum of squared differences between the tissue TACs and the model-predicted curves. The model with the lowest Akaike information criterion (AIC) value was chosen. The AIC is calculated as follows:

$$\mathrm{AIC} = n * \Sigma w(\gamma - \gamma_1)^2 + 2 * p$$

with n, number of observations (image frames); w, weighting factor (Gaussian); γ, calculated data; γ_1 = measured data; p, number of constants.

A two-tissue compartment model best characterized the tumor and mucosa data. In muscle tissue, it was difficult to resolve the second compartment, therefore, a one-tissue compartment model was used for further analysis of this tissue. The total distribution volume (DV_{tot}) was calculated for all ROIs based on the directly estimated kinetic rate constants (K_1-k_4) and the estimated fraction of blood volume V_B according to the formula:

$$\mathrm{DV}_{tot} = \frac{K_1}{k_2} * \left(1 + \frac{k_3}{k_4}\right)(\text{two} - \text{tissue compartment model}) \; or$$

$$\mathrm{DV} = \frac{K_1}{k_2}(\text{one} - \text{tissue compartment model})$$

A more detailed description of the compartment models can be found elsewhere (26–28).

Collection of tissue samples and immunohistochemistry

In patients eligible for tumor resection (n = 7), fresh-frozen tissue samples from the tumors were obtained in the operating room from tumor regions with maximum tracer uptake. The mean time interval between PET and operation was 3.2 days. Both the surgeons and a member of the department of nuclear medicine (A.J. Beer) were present in the operating room for collection of the tissue samples, and both were aware of the imaging findings of the PET scan, which were shown and discussed the day before the operation. The specimens were snap-frozen in liquid nitrogen and stored at -70°C until staining was done.

For immunohistochemical investigation, frozen tumor tissues were sectioned (6 μm) and stained using the biotinylated monoclonal anti-αvβ3 antibody LM609 (1:100; Chemicon Europe). Sections were processed by peroxidase staining (peroxidase substrate KIT AEC; Vector Laboratories).

Light microscopic evaluation of the patterns of staining (staining of endothelium of microvessel and/or tumor cells) was done by one senior pathologist (M. Sarbia), who was blinded to the clinical results of the results of SUV measurements. Intensity of staining was graded on a four-point scale from 0 to +++ (missing, weak, moderate, or intense staining) as described previously (17).

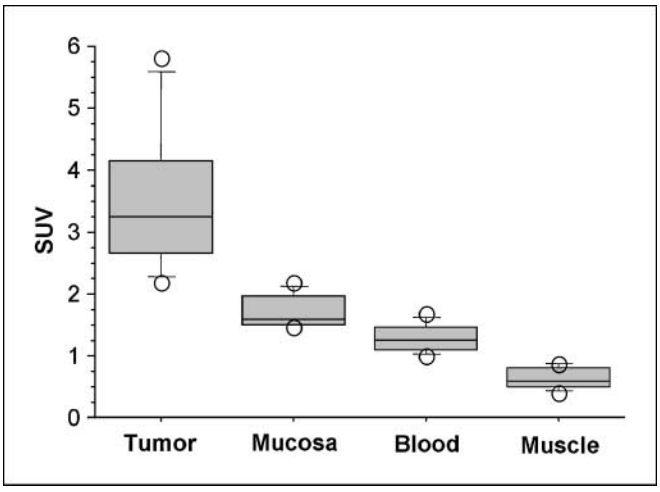

Fig. 1. Box plot diagram of the mean SUVs of tumors and normal tissue (oral mucosa, muscle, and blood pool) from the static emission scans. Tumor uptake was very heterogeneous but usually higher than uptake in background tissue, resulting in good image contrast.

Image fusion and determination of tumor subvolumes

For image fusion, PET data of the attenuation-corrected static emission scans from the ECAT Exact scanner were first converted to DICOM format by using the EcatConverter software. Next, data were manually fused with the corresponding MRI or MSCT scans of the head-and-neck area using the iPlan 2.0 software (BrainLAB). Three or more reference anatomic landmarks (e.g., parotid and submandibular gland, hard and soft palate, skin contour) were matched and fused, with a maximum acceptable error of 5 mm. For imaging fusion, T1-weighted unenhanced MRI scans (n = 6) or contrast-enhanced MSCT scans (n = 2) were used. For definition of the tumor boundaries and the gross tumor volume, either T1-weighted fat-saturated gadolinium-enhanced MRI sequences, STIR sequences, or contrast-enhanced MSCT scans were used, respectively, depending on which modality delineated the tumor best. Next, a threshold of SUV 3.0 was applied to the PET data sets, so that only areas in the scan with SUVs >3.0 were visible. All visible voxels within the gross tumor volume on the fusion images were then marked and the subvolume of these voxels taken together was calculated. This was done to define a biological subvolume of the tumor with more intense $\alpha v\beta 3$ expression. The threshold of 3.0 was chosen according to the results of former studies, in which all tumors with SUVs >3.0 showed at least intermediate or intense $\alpha v\beta 3$ expression (18). Image fusion and definition of gross tumor volume was done in consensus by a board-certified radiologist with experience in oncological PET and PET/CT imaging (A.J. Beer) and by a board-certified radiation therapist with experience in combined modality imaging (A.L. Grosu).

Statistical analysis

All quantitative data are expressed as mean ± 1 SD. The correlation between quantitative variables was evaluated by the Wilcoxon test. Statistical significance was tested by using ANOVA.

All statistical tests were done at the 5% level of statistical significance, using the StatView program (SAS Institute Inc.) or MedCalc (version 6.15.000).

Results

Static emission scans. Ten of 12 tumors could be identified by [^{18}F]Galacto-RGD PET. The two tumors missed were <5 mm and were identified by clinical examination as small superficial lesions but were not identified by MSCT or MRI imaging either. The mean size of all tumors as determined by histopathologic analysis (n = 7) or MRI (n = 4) was 1.86 ± 1.13 cm. Tumor size and tumor SUV were not correlated with each other (P = 0.63, R = 0.19). [^{18}F]Galacto-RGD PET identified two of six patients with pathologically proven lymph node metastasis (n = 4) or clinically suspected lymph node metastasis (n = 2); the maximum diameter of the missed pathologically proven lymph node metastasis was 10 and 14 mm. In one patient, distant

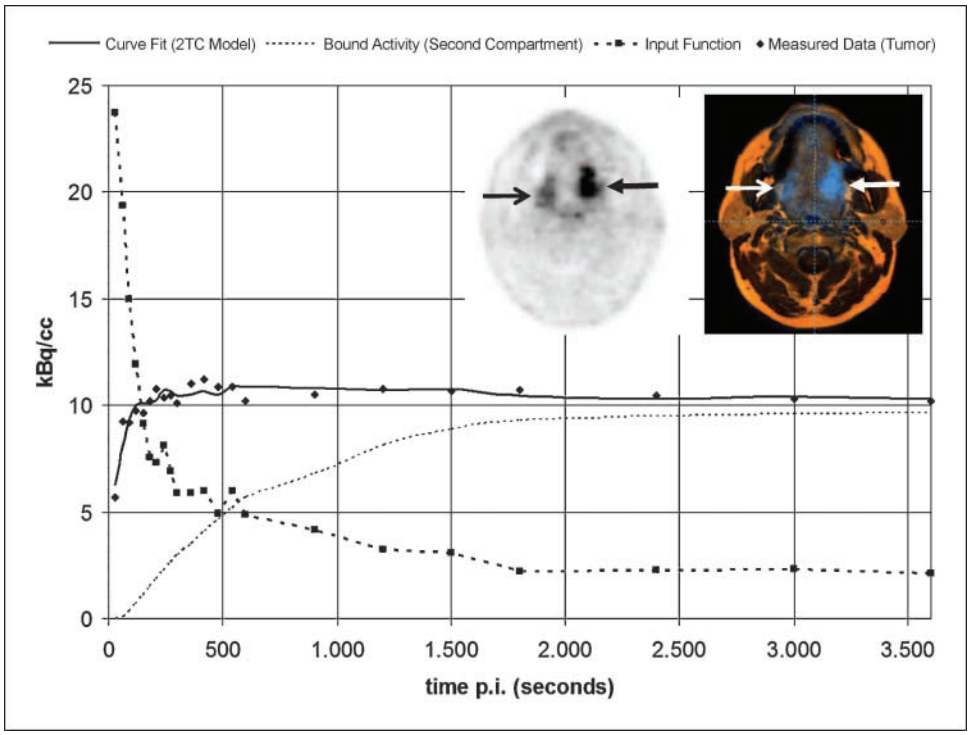

Fig. 2. Representative dynamic study with kinetic modeling using a two-tissue compartment model (*2TC model*) of a patient with two simultaneous SCCHN (*arrows*). Insets, axial slices of the [^{18}F]Galacto-RGD PET and PET/MRI image fusion (*top right*). There is rapid tracer washout from the blood pool, whereas activity in the tumor increases during the first minutes and then plateaus. Dotted line, the amount of bound activity in the second compartment, which is high and also reaches a plateau after ~30 min of scanning.

Table 2. Kinetic modeling data

	DV_{tot}	CoV
Tumors	2.95 ± 1.51	7.02 ± 2.76
Mucosa	1.82 ± 0.35	6.54 ± 2.52
Muscle	0.37 ± 0.09	4.99 ± 1.58

NOTE: Values are presented as mean values ± SD (n = 6).
Abbreviations: CoV, coefficient of variation (%); DV_{tot}, total distribution volume.

metastases to the lung identified by [^{18}F]FDG-PET/CT were not identified by [^{18}F]Galacto-RGD PET.

The results of the SUV measurements for tumors, muscle, oral mucosa, and blood pool are summarized in Fig. 1. The mean SUV for tumors was 3.4 ± 1.2, 1.29 ± 0.22 for blood, 1.71 ± 0.25 for oral mucosa, 1.64 ± 0.35 for the submandibular gland, 1.13 ± 0.17 for the parotid gland, and 0.64 ± 0.17 for muscle. The tumor/blood ratio and tumor/muscle ratio was calculated to be 2.79 ± 1.08 and 5.51 ± 1.56, respectively.

Dynamic scans and kinetic modeling. In all dynamic scans, tumors showed rapid tracer accumulation during the first 10 to 15 min, followed by a plateau phase with either no or only a slight decrease of activity until 60 min p.i. (Fig. 2). The results of the modeling data are summarized in Table 2. The two-tissue compartment model (mean AIC, 92.0 ± 15.92) fitted significantly better for tumors than the one-tissue compartment model (mean AIC, 115.0 ± 10.52; $P < 0.05$). The fraction of blood volume V_B was calculated to be 0.21 ± 0.16. For muscle, the one-tissue compartment model fits the data best. DV_{tot} values for tumors were always higher than the DV_{tot} for muscle and for mucosa with a mean ratio of 7.97 and 1.62 for tumors relative to muscle and mucosa, respectively.

Immunohistochemistry. αvβ3 expression could be confirmed by immunohistochemistry in all primary tumor specimens. In six of seven specimens, αvβ3 expression was identified predominantly on the endothelium of newly formed blood vessels (Fig. 3). In one specimen, αvβ3 expression could also be seen on the tumor cells themselves in addition to staining of the neovasculature. The median SUV in samples with weak αvβ3 expression was 3.1 (n = 3), the median SUV in samples with moderate αvβ3 expression was 4.6 (n = 4), however, due to the low number of samples, the difference did not reach statistical significance ($P > 0.1$). Unfortunately, no samples from the two tumors and the malignant lymph nodes missed by imaging could be obtained. In samples of benign lymph nodes, no substantial αvβ3 expression could be seen, except for staining of scattered cells, which were probably macrophages. In one lymph node metastasis, prominent staining of the neovasculature was seen.

Image fusion and definition of tumor subvolumes. Image fusion of [^{18}F]Galacto-RGD PET and MRI and/or MSCT scans were feasible in all cases (n = 8) within the maximum acceptable error of 5 mm mismatch. The mean gross tumor

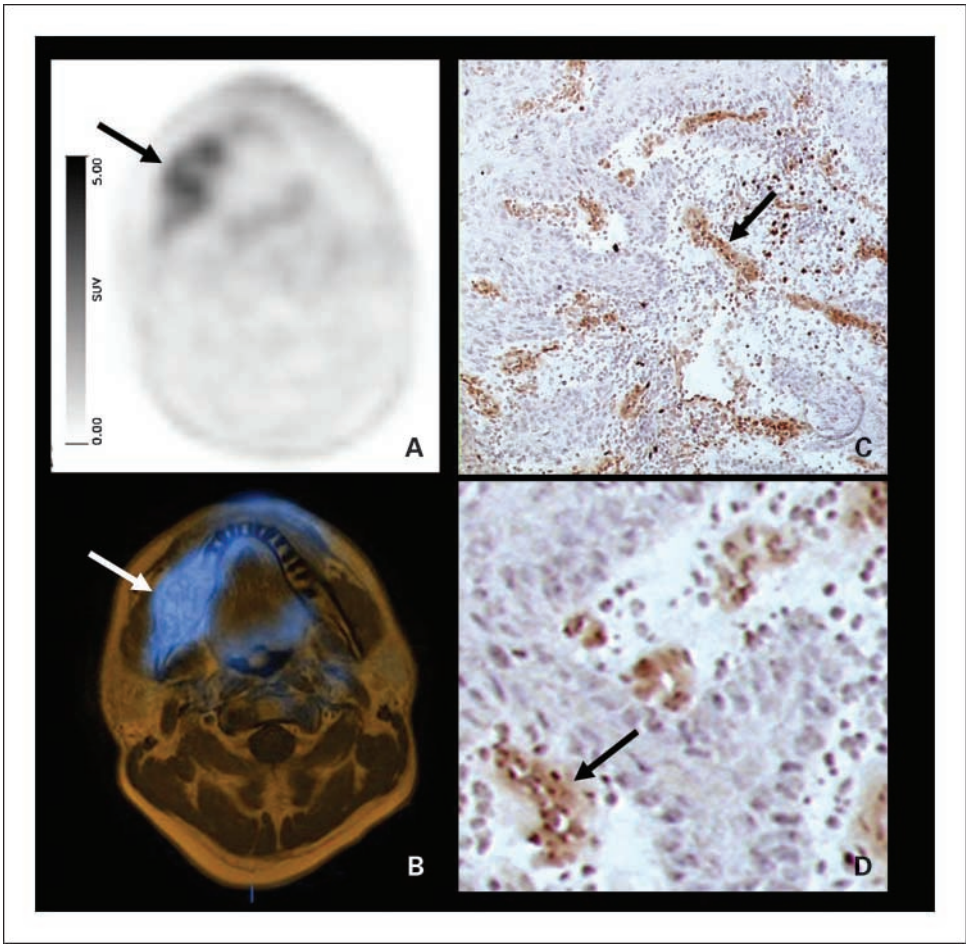

Fig. 3. Patient with a SCCHN in the right mandible (*arrows, A* and *B*). [^{18}F]Galacto-RGD PET (*A*) and PET/MRI image fusion (*B*) show heterogeneous intense tracer accumulation in the lesion, whereas there is only low background uptake in parts of the oral cavity and very low uptake in the parotid glands and in muscle tissue. Immunohistochemical evaluation of αvβ3 expression at low-power magnification (*C*) and at high-power magnification (*D*) shows intense staining of the neovasculature (*arrows*) without staining of the tumor cell complexes.

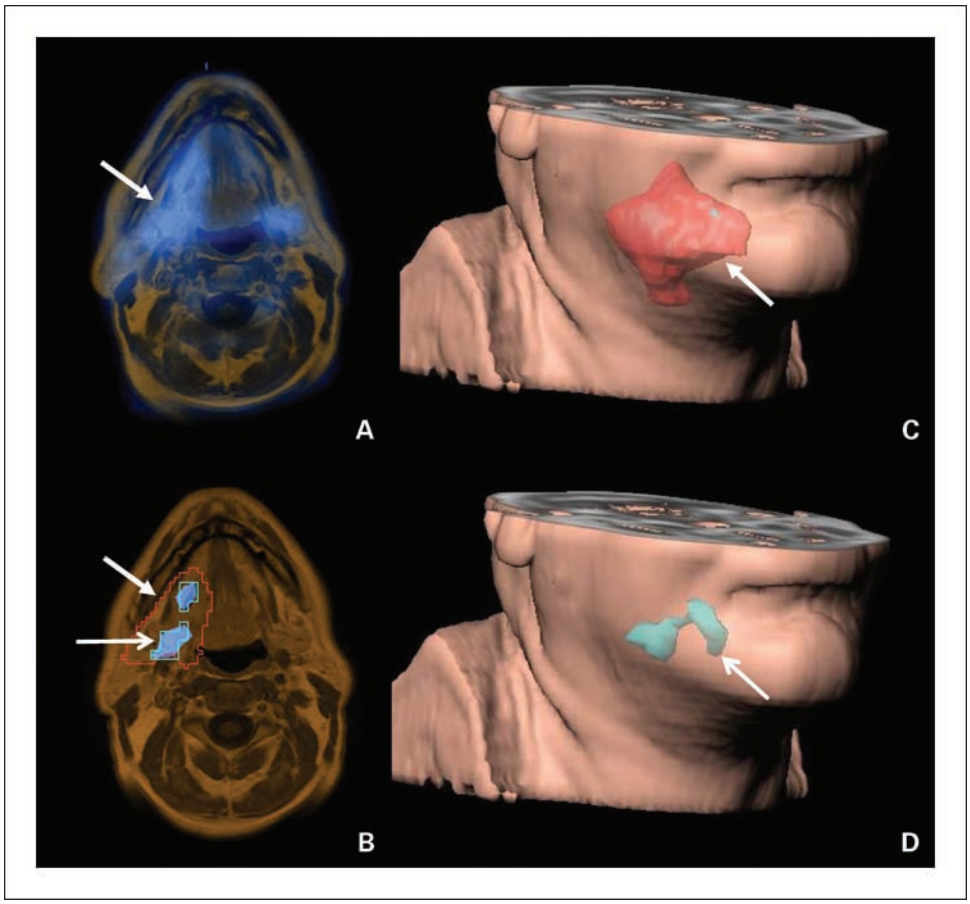

Fig. 4. Patient with a SCCHN in the right oral cavity. The [18F]Galacto-RGD PET/MRI image fusion (*A*) shows intense and heterogeneous tracer uptake in the lesion (*arrow*). Moderate uptake is also notable in the submandibular gland. A transaxial MRI slice of the tumor volume as defined by MRI (*B, closed-tipped arrow; red line*) and in the corresponding three-dimensional reconstruction (*C, closed-tipped arrow*). By applying a threshold of SUV = 3 and only using pixels with SUVs above this threshold, a subvolume with more intense αvβ3 expression could be defined (*blue line* and *blue area, B; open-tipped arrow*), (*D, blue volume; open-tipped arrow*).

volume was 26.4 ± 20.2 cm^3 (range, 0-59.6 cm^3). The mean tumor subvolume with SUVs >3.0 was 3.4 ± 3.4 cm^3 (range, 0-9 cm^3) or 13.1 ± 11.7% of the gross tumor volume (range, 0–38%; Fig. 4).

Discussion

In this study, we showed the feasibility of PET imaging of αvβ3 expression in SCCHN patients with good contrast using [^{18}F]Galacto-RGD. The kinetic modeling data are compatible with slowly reversible specific receptor binding. Immunohistochemistry confirmed αvβ3 expression predominantly on the neovasculature. Image fusion with MRI or MSCT data sets was possible and tumor subvolumes with more intense tracer uptake could be successfully defined.

The biodistribution data showed very low tracer uptake in the background and muscle tissue with high tumor/muscle ratios, resulting in good image contrast and easy delineation of most lesions. There was some uptake notable in the salivary glands, which was also low and did not interfere with the diagnosis or analysis of pathologic uptake in tumors. The uptake in oral mucosa was somewhat higher than in muscle or salivary glands but was still lower than the uptake in the majority of tumor lesions. In two patients, small lesions (<5 mm) were missed by [^{18}F]Galacto-RGD PET, which was probably related to the limited spatial resolution of a clinical PET scanner, which is in the range of 5 to 6 mm (29). Two of four pathologically proven lymph node metastases were also missed by [^{18}F]Galacto-RGD PET. However, we could not obtain tissue samples from the missed tumors and lymph nodes, therefore, the question if the failure to depict these lesions was a result of technical problems or due to a reflection of vascular biology has to be evaluated in future studies.

The TACs of the tumors derived from the dynamic scans showed a plateau phase after ~15 min p.i. after an initial increase of activity and no or only minimal decrease of activity until the end of the measurement at 60 min p.i. The kinetic modeling data for tumors showed that a two-tissue compartment model fitted best, moreover, the DV_{tot} values for tumors were always substantially higher than for muscle or mucosa, which taken together, suggests specific receptor binding of the tracer. It has to be stressed, however, that for truly quantitative measurements of rate constants and receptor density, kinetic modeling using arterial blood sampling would still be necessary, because image-based input functions from small vessels like the carotid arteries lead to an underestimation of the peak plasma activity, and consequently, an overestimation of the fractional blood volume V_B and K_1 (30).

Immunohistochemistry confirmed αvβ3 expression predominantly on the neovasculature in SCCHN. Maximum staining intensity in immunohistochemistry in this study was lower compared with those samples from our previous studies which showed αvβ3 expression on vasculature as well as on tumor cells (16, 17). Only in one tumor specimen, tumor cells were stained in addition to endothelial cells in the neovasculature. This is important information because our previous studies as well as data in the literature show, that substantial αvβ3 expression could be found on tumor cells as well in some

tumor types, e.g., in melanoma (16, 31). Thus, in these tumors, the signal of [^{18}F]Galacto-RGD PET represents a combination of $\alpha v\beta 3$ expressed in the neovasculature and in tumor cells, and might not be an optimal surrogate variable of angiogenesis in such cases. Our results suggest that due to the predominant $\alpha v\beta 3$ expression on the neovasculature, this should not be a problem with SCCHN. The role of $\alpha v\beta 3$ has been examined intensively in the last few years and besides its role in tumor cell migration and metastasis, it is supposed to be a marker of angiogenic vessels but not of resting vessels (32). We therefore conclude that $\alpha v\beta 3$ expression is promising as a marker of angiogenesis in SCCHN and that [^{18}F]Galacto-RGD PET might be used as a surrogate variable of angiogenic activity. However, it has to be mentioned that contradictory reports about the role of $\alpha v\beta 3$ exist as well and that the ultimate meaning of $\alpha v\beta 3$ expression in the context of angiogenesis is very complex and still has to be examined more thoroughly in the future (33). Currently, $\alpha v\beta 3$ is assumed to have a positive and a negative regulatory role in angiogenesis, depending on the respective biological context. Due to the low number of samples in our study, and due to the small size of the specimens, no exact evaluation of the microvessel density was feasible. This was due to the overall small size of the tumors eligible for resection which limited the sampling of fresh-frozen tissue without compromising the conventional histologic workup of the tumors. Consequently, no exact correlation of $\alpha v\beta 3$ expression in immunohistochemistry and [^{18}F]Galacto-RGD uptake was possible, which is a limitation of our study.

Image fusion with morphologic imaging data sets from MRI and/or MSCT was feasible, albeit patients were scanned without mask fixation. We showed that the image quality of a [^{18}F]Galacto-RGD PET scan allows for adequate manual fusion with MRI or MSCT using anatomic landmarks. Mismatches were notable, particularly at the dorsal part of the neck where the skin contour and folds were different due to the different gantry tables used in MRI and PET. For actual radiation treatment planning, laser visors, external markers, and immobilization devices would have to be used to facilitate image fusion and to get optimum results (34).

In summary, assessment of angiogenesis with [^{18}F]Galacto-RGD PET in SCCHN seems feasible and might be used in the future for planning and response evaluation of antiangiogenic therapies combined with chemotherapy and/or radiotherapy.

Acknowledgments

We thank the Cyclotron and PET team, especially Michael Herz, Gitti Dzewas, and Coletta Kruschke for excellent technical assistance.

References

1. Kerbel RS. Antiangiogenic therapy: a universal chemosensitization strategy for cancer? Science 2006; 312:1171–5.
2. Hurwitz H, Fehrenbacher L, Novotny W, et al. Bevacizumab plus irinotecan, fluorouracil, and leucovorin for metastatic colorectal cancer. N Engl J Med 2004; 350:2335–42.
3. McGinn CJ, Shewach DS, Lawrence TS. Radiosensitizing nucleosides. J Natl Cancer Inst 1996;88: 1193–203.
4. Stratford IJ. Concepts and developments in radiosensitization of mammalian cells. Int J Radiat Oncol Biol Phys 1992;22:529–32.
5. Ma BB, Bristow RG, Kim J, Siu LL. Combined-modality treatment of solid tumors using radiotherapy and molecular targeted agents. J Clin Oncol 2003;14: 2760–76.
6. Baumann M, Krause M, Zips D, et al. Molecular targeting in radiotherapy of lung cancer. Lung Cancer 2004;45:187–97.
7. Teicher BA, Holden SA, Dupuis NP, et al. Antiangiogenic agents can increase tumor oxygenation and response to radiation therapy. Radiat Oncol Invest 1995;2:269–76.
8. Zips D, Eicheler W, Geyer P, et al. Enhanced susceptibility of irradiated tumor vessels to vascular endothelial growth factor receptor tyrosine kinase inhibition. Cancer Res 2005;65:5374–9.
9. Dicker AP, Anne R, Bonanni R, et al. Phase I trial results of recombinant human angiostatin protein (rhA) and external beam radiation therapy (EBRT) [abstract]. 38th Annual Meeting of the American Association of Clinical Oncology. Alexandria (VA): ASCO Publications; 2002.
10. Hood JD, Cheresh DA. Role of integrins in cell invasion and migration. Nat Rev Cancer 2002;2:91–100.
11. Ruoslahti E. Specialization of tumor vasculature. Nat Rev Cancer 2002;2:83–90.
12. Albert JM, Cao C, Geng L, et al. Integrin $\alpha v\beta 3$ antagonist Cilengitide enhances the efficacy of radiotherapy in endothelial cell and non-small-cell lung cancer models. Int J Rad Oncol Biol Phys 2006;65: 1536–43.
13. Haubner R, Wester HJ, Weber WA, et al. Noninvasive imaging of $\alpha(v)\beta 3$ integrin expression using 18F-labeled RGD-containing glycopeptide and positron emission tomography. Cancer Res 2001;61:1781–5.
14. Beer AJ, Haubner R, Goebel M, et al. Biodistribution and pharmacokinetics of the $\alpha v\beta 3$ selective tracer 18F Galacto-RGD in cancer patients. J Nucl Med 2005; 46:1333–41.
15. Beer AJ, Haubner R, Wolf I, et al. PET-based human dosimetry of 18F-galacto-RGD, a new radiotracer for imaging $\alpha v\beta 3$ expression. J Nucl Med 2006;47: 763–9.
16. Haubner R, Weber WA, Beer AJ, et al. Non-invasive visualization of the activated $\alpha v\beta 3$ integrin in cancer patients by positron emission tomography and [^{18}F]Galacto-RGD. PLoS Med 2005;2:e70.
17. Beer AJ, Haubner R, Sarbia M, et al. Positron emission tomography using [^{18}F]Galacto-RGD identifies the level of integrin $\alpha(v)\beta 3$ expression in man. Clin Cancer Res 2006;12:3942–9.
18. Zatterstrom UK, Brun E, Willen R, Kjellen E, Wennerberg J. Tumor angiogenesis and prognosis in squamous cell carcinoma of the head and neck. Head Neck 1995;17:312–8.
19. O-charoenrat P, Rhys-Evans P, Eccles SA. Expression of vascular endothelial growth factor family members in head and neck squamous cell carcinoma correlates with lymph node metastasis. Cancer 2001;92:556–68.
20. Erovic BM, Neuchrist C, Berger U, El-Rabadi K, Burian M. Quantitation of microvessel density in squamous cell carcinoma of the head and neck by computer-aided image analysis. Wien Klin Wochenschr 2005;117: 53–7.
21. Haubner R, Kuhnast B, Mang C, et al. [^{18}F]Galacto-RGD: synthesis, radiolabeling, metabolic stability, and radiation dose estimates. Bioconjug Chem 2004;15: 61–9.
22. Weber WA, Ziegler SI, Thodtman R, Hanauske AR, Schwaiger M. Reproducibility of metabolic measurements in malignant tumors using FDG PET. J Nucl Med 1999;40:1771–7.
23. Brix G, Bellemann ME, Hauser H, Doll J. Recovery coefficients for the quantification of the arterial input functions from dynamic PET measurements: experimental and theoretical determination. Nuklearmedizin 2002;41:184–90.
24. Schiepers C, Chen W, Dahlbom M, Cloughesy T, Hoh CK, Huang SC. (18) F-fluorothymidine kinetics of malignant brain tumors. Eur J Nucl Med Mol Imaging 2007;34:1003–11.
25. Chen K, Bandy D, Reiman E, et al. Noninvasive quantification of the cerebral metabolic rate for glucose using positron emission tomography, 18F-fluoro-2-deoxyglucose, the Patlak method, and an image-derived input function. J Cereb Blood Flow Metab 1998;18:716–23.
26. Carson RE. Tracer Kinetic Modelling in PET. In: Valk PE, Bailey DL, Townsend DW, Maisey MN, editors. Positron emission tomography—basic science and clinical practice. 2nd ed. London: Springer-Verlag; 2003. p. 147–80.
27. Slifstein M, Laruelle M. Models and methods for derivation of *in vivo* neuroreceptor parameters with PET and SPECT reversible radiotracers. Nucl Med Biol 2001;28:595–608.
28. Spilker ME, Sprenger T, Valet M, et al. Quantification of [^{18}F]diprenorphine kinetics in the human brain with compartmental and non-compartmental modeling approaches. Neuroimage 2004;22:1523–33.
29. Weber WA. Positron emission tomography as an imaging biomarker. J Clin Oncol 2006;24:3282–92.
30. Krohn KA, Mankoff DA, Muzi M, Link JM, Spence AM. True tracers: comparing FDG with glucose and FLT with thymidine. Nucl Med Biol 2005;32:663–71.
31. Felding-Habermann B, Fransvea E, O'Toole TE, Manzuk L, Faha B, Hensler M. Involvement of tumor cell integrin $\alpha v\beta 3$ in haematogenous metastasis of human melanoma cells. Clin Exp Metastasis 2002; 19:427–36.
32. Brooks PC, Clark RAF, Cheresh DA. Requirement of vascular integrin $\alpha v\beta 3$ for angiogenesis. Science 1994;2674:569–71.
33. Hynes RO. A reevaluation of integrins as regulators of angiogenesis. Nat Med 2002;8:918–21.
34. Rajendran JG, Hendrickson KR, Spence AM, Muzi M, Krohn KA, Mankoff DA. Hypoxia imaging-directed radiation treatment planning. Eur J Nucl Med Mol Imaging 2006;33:44–53.